

Variable Substitution and Bilinear Programming for Aligning Partially Overlapping Point Sets

Wei Lian^a, Zhesen Cui^a, Fei Ma^a, Hang Pan^a, Wangmeng Zuo^b

^aDepartment of Computer Science, Changzhi University, Changzhi, Shanxi, China, 046011

^bSchool of Computer Science and Technology, Harbin Institute of Technology, Harbin 150001, China

Abstract

In many applications, the demand arises for algorithms capable of aligning partially overlapping point sets while remaining invariant to the corresponding transformations. This research presents a method designed to meet such requirements through minimization of the objective function of the robust point matching (RPM) algorithm. First, we show that the RPM objective is a cubic polynomial. Then, through variable substitution, we transform the RPM objective to a quadratic function. Leveraging the convex envelope of bilinear monomials, we proceed to relax the resulting objective function, thus obtaining a lower bound problem that can be conveniently decomposed into distinct linear assignment and low-dimensional convex quadratic program components, both amenable to efficient optimization. Furthermore, a branch-and-bound (BnB) algorithm is devised, which solely branches over the transformation parameters, thereby boosting convergence rate. Empirical evaluations demonstrate better robustness of the proposed methodology against non-rigid deformation, positional noise, and outliers, particularly in scenarios where outliers remain distinct from inliers, when compared with prevailing state-of-the-art approaches.

Keywords: branch-and-bound, partial overlap, bilinear monomial, point set registration, convex envelope, linear assignment

1. Introduction

Aligning 2D/3D point sets is crucial across computer vision, robotics, and remote sensing applications. Apart from disturbances like non-rigid deformation and positional noise, this task becomes especially challenging when the two point sets only partial overlap and lack initial coarse alignment.

A practical approach to addressing the point set registration challenge involves minimizing the RPM objective [1]. This objective is characterized by a mixed linear assignment-least squares formulation:

$$E(P, \theta) = \sum_{i,j} p_{ij} \|y_j - \mathbf{T}(x_i|\theta)\|^2$$

Here, x_i and y_j represent two point sets intended for alignment, $p_{ij} \in \{0, 1\}$ indicates point correspondence, and \mathbf{T} denotes a spatial transformation parameterized by θ . Lian *et al.* demonstrated that in scenarios where one point set can be embedded within another, after spatial transformations are eliminated, the RPM objective can be reduced to a concave quadratic function of point correspondence, exhibiting a low-rank structure [2]. This simplification facilitates the implementation of efficient branch-and-bound (BnB) based global optimization strategies.

The algorithm introduced in [2] is extended to handle partial overlap in [3]. Here, the objective function takes the form

of a non-quadratic concave function of point correspondence variable, exhibiting a low-rank structure. This structure enables application of efficient BnB optimization techniques. However, the algorithm's branching space is a projected space of point correspondence, characterized by a dimensionality surpassing that of the transformation parameters. This results in a slower convergence rate for the method. Additionally, to ensure concavity of the objective function over the initial bounding region, the method requires the regularization of transformations, which in turn demands prior knowledge of transformation parameters. Consequently, the method lacks invariance to corresponding transformations, presenting a notable drawback.

In response to this challenge, Lian and Zhang utilized the inherent constraints of rigid transformations to devise a novel objective function for the point correspondence variable. This function exhibits concavity across the entire solution space, eliminating the need for regularization of transformations [4]. Alternatively, Lian *et al.* employed the polyhedral annexation (PA) algorithm to minimize the RPM objective [5]. PA offers an advantage over BnB by operating exclusively within the concavity region of the objective, thus eliminating the need for transformation regularization. However, both approaches [4] and [5] still face the challenge inherited from [3] of branching within a high-dimensional projected space of point correspondence, resulting in sluggish convergence rates.

The methods mentioned above all share a common practice: they remove spatial transformations from the RPM objective, resulting in a function based solely on point correspondence variable. However, this simplification leads to a complex function, posing challenges such as high-dimensional branch-

Email addresses: lianwei@czc.edu.cn (Wei Lian),
cuizhesen@gmail.com (Zhesen Cui), mafei@czc.edu.cn (Fei Ma),
panhang@czc.edu.cn (Hang Pan), cswmzuo@gmail.com (Wangmeng Zuo)

$$\begin{aligned}
E(\mathbf{P}, \theta) &= \boxed{\text{trilinear term of } \theta \text{ and } \mathbf{P}} + \text{quadratic term of } \theta + \text{bilinear term of } \theta \text{ and } \mathbf{P} + \text{linear term of } \mathbf{P} \\
&\quad \text{define } \downarrow \Theta \triangleq \theta\theta^T \\
E(\mathbf{P}, \Theta, \theta) &= \boxed{\text{bilinear term of } \Theta \text{ and } \mathbf{P}} + \text{quadratic term of } \theta + \boxed{\text{bilinear term of } \theta \text{ and } \mathbf{P}} + \text{linear term of } \mathbf{P} \\
&\quad \text{bilinear } \downarrow \text{relaxation} \qquad \qquad \qquad \text{bilinear } \downarrow \text{relaxation} \\
E_l(\mathbf{P}, \Theta, \theta) &= \boxed{\text{linear term of } \Theta \text{ and } \mathbf{P}} + \text{quadratic term of } \theta + \boxed{\text{linear term of } \theta \text{ and } \mathbf{P}} + \text{linear term of } \mathbf{P} \\
&\quad \text{substitute } \downarrow \text{back } \Theta = \theta\theta^T \\
E_l(\mathbf{P}, \theta) &= \text{quadratic term of } \theta + \text{linear term of } \theta + \text{linear term of } \mathbf{P}
\end{aligned}$$

Figure 1: Derivation of a lower bound function of the RPM objective function via variable substitution and bilinear relaxation.

ing spaces and intricate optimization strategies. An alternative approach, as demonstrated by [6], suggests retaining spatial transformations. In this method, trilinear and bilinear relaxation are employed to derive a lower bound function. This approach offers several advantages, including its ability to handle partial overlap, its invariance to corresponding transformations, and its utilization of a low-dimensional branching space.

Following the approach outlined in [6], we introduce a new Branch-and-Bound (BnB) algorithm tailored for optimizing the RPM objective function. This algorithm boasts the following features:

- The algorithm proposed by [6] is complex because it necessitates reformulating the RPM objective function to ensure that one of the variables within the trilinear monomial includes the origin within its range. In contrast, as illustrated in Fig. 1, our method exclusively utilizes bilinear relaxation to establish the lower bound function, eliminating the necessity to fulfill this condition. This results in a streamlined algorithm compared to [6].
- The optimization of the lower bound function can be broken down into two distinct tasks: linear assignment and low-dimensional convex quadratic optimization related to spatial transformation variables. Both of these tasks can be efficiently solved with global optimality assurances.
- Our approach inherits the advantageous characteristics outlined in [6], including its ability in handling partial overlap, invariance to corresponding transformations, and utilization of a low-dimensional branching space.

The paper is structured as follows: We begin with a review of related work (Sec. 2). Following that, we introduce the theoretical framework necessary for developing our lower bound functions (Sec. 3). Next, we delve into our objective function (Sec. 4 and optimization strategy (5). Subsequently, we apply the proposed algorithm to 2D and 3D registration (Sec. 6 and Sec. 7). Finally, we present our experimental results (Sec. 8) and conclude the paper (Sec. 9).

2. Related work

A comprehensive survey of point set registration methods is available in [7]. Here, we focus solely on works closely related

to ours.

2.1. Local methods

Simultaneous pose and correspondence. The widely known ICP method [8] iterates between recovering point correspondence and updating spatial transformation. Despite its efficiency, the discrete nature of point correspondence often traps the method in local minima. Zhang *et al.* enhanced the robustness of ICP by constraining the rotation angle at each iterative step [9]. Liang introduced RGB information to the registration process of ICP [10]. The RPM method [1] relaxes point correspondence to be fuzzily valued and employs deterministic annealing (DA) to gradually recover point correspondence. Instead of DA, Sofka *et al.* utilized the covariance matrix of the transformation parameters to determine the fuzziness of point correspondence, resulting in better robustness to missing or extraneous structures [11]. Ma *et al.* employed L2E to robustly estimate transformation for non-rigid registration [12]. Our method is related to the aforementioned methods by also modeling spatial transformation and correspondences. However, our objective function is globally minimized, which enhances our method’s robustness to disturbances.

Correspondence-free methods. The CPD method [13] frames point matching as fitting a Gaussian mixture model (GMM) representing one point set to another. GMMREG [14] utilizes two GMMs to represent two point sets and minimizes the L_2 -norm distance between them. The SVGMS method represents point sets using sparse Gaussian components [15]. Efficiency in GMM-based methods is enhanced by employing filtering to solve the correspondence problem [16]. The density variation problem of point sets is addressed in [17] by modeling scene structure. Hierarchical Gaussian mixture representation improves speed and accuracy of registration [18].

2.2. Global methods

BnB based methods. The Branch-and-Bound (BnB) algorithm stands as a widely-used global optimization technique. Rooted in Lipschitz theory, BnB is applied to align 3D shapes [19], albeit with limitations regarding outliers or occlusions. By capitalizing on the structure of 3D rigid motions geometry, Go-ICP [20] globally optimizes the objective of ICP. GOGMA [21] achieves point set registration by aligning Gaussian Mixture

Models (GMMs) constructed from the original point sets. Employing stereographic projection, the fast rotation search (FRS) method efficiently recovers 3D rotation between two point sets [22]. Bayesian nonparametric mixture and a novel approach of tessellating rotation space are introduced in [23], leading to an efficient alignment algorithm. Our BnB-based method distinguishes itself from the aforementioned methods by also incorporating point correspondences. This feature empowers our method to better handle non-rigid deformation.

Mismatch removal methods. An alternative avenue of research focuses on recovering spatial transformations given putative point correspondences. The fast global registration (FGR) method [24] optimizes a robust objective grounded in the duality between line processes and robust estimation. GORE [25] eliminates a large portion of outliers using geometric operations before invoking RANSAC. TEASER++ [26] employs a graph-theoretic approach to decouple rotation, scale, and translation estimation. It adopts a truncated least squares formulation for each subproblem, enabling effective mismatch removal.

2.3. Deep learning methods

Correspondence-free methods. The Lucas–Kanade algorithm aligns global features of point sets generated by a PointNet network in [27]. This approach is refined in [28] by employing a decoder to convert the generated global features back into point sets. Ensuring fidelity, Chamfer distances between the decoded point sets and the original ones are minimized.

Correspondence-based methods. The FCGF method [29] employs sparse high-dimensional convolutions to extract dense feature descriptors from point clouds. This method significantly outperforms many hand-crafted features and PointNet-based methods. Additionally, it surpasses a 3D convolution-based method [30]. The deep global registration method [31] utilizes FCGF feature descriptors for point cloud registration. DCP [32] utilizes DGCNN [33] and Transformer [34] to extract features for each point set, with SVD employed to recover rigid transformation. PRNet [35] extends DCP to handle partially overlapping point sets iteratively. IDAM [36] considers both geometric and distance features during its point matching process. RIENet [37] calculates feature-to-feature correspondences with neighborhood consensus. Finally, [38] performs partial point set registration by generating matching credibility on the global semantic level and learning geometric features on the local structural level.

3. Bilinear convex envelope linearization

The convex envelope of a bilinear monomial xy subject to constraints $\underline{x} \leq x \leq \bar{x}$ and $\underline{y} \leq y \leq \bar{y}$ can be described as:

$$\begin{cases} (xy)_{l1} \triangleq \underline{xy} + x\bar{y} - \underline{x}\bar{y} \leq xy, \\ (xy)_{l2} \triangleq \bar{xy} + x\underline{y} - \bar{x}\underline{y} \leq xy \end{cases} \quad (1)$$

There are two ways of utilizing this formula when devising the lower bound problem: (1) Integration of the term

$\max\{(xy)_{l1}, (xy)_{l2}\}$ into the lower bound objective function. Nevertheless, this incorporation can lead to non-linearity of the resultant function. (2) Formulation of a subproblem in the format $\min\{\alpha | \alpha \geq (xy)_{l1}, \alpha \geq (xy)_{l2}\}$ within the lower bound problem. However, this approach increases the complexity of constraints and raises concerns regarding the feasibility of the resulting problem for efficient optimization via combinatorial optimization algorithms.

Hence, in alignment with the methodology proposed in [6], we advocate for using the average of the convex envelope components, as delineated in (2):

$$(xy)_l \triangleq \frac{1}{2} \sum_i (xy)_{li} \leq xy \quad (2)$$

as the lower bound function for xy . This choice has the advantage that the lower bound function is linear, thereby facilitating efficient optimization by combinatorial optimization algorithms.

[6] also shows that for $(xy)_l$ to converge to xy , we only need to branch over one variable x or y that makes up the bilinear monomial xy . This is a crucial property and the good convergence of the proposed algorithm hinges on this fact.

4. Problem formulation

Suppose there are two point sets $\mathcal{X} = \{\mathbf{x}_i, 1 \leq i \leq n_x\}$ and $\mathcal{Y} = \{\mathbf{y}_j, 1 \leq j \leq n_y\}$ in \mathbb{R}^{n_d} to be aligned, where the column vectors \mathbf{x}_i and \mathbf{y}_j represent the coordinates of points i and j , respectively. Based on [3], this problem can be modeled as a mixed linear assignment–least square problem:

$$\min E(\mathbf{P}, \boldsymbol{\theta}) = \sum_{i,j} p_{ij} \|\mathbf{y}_j - \mathbf{J}(\mathbf{x}_i)\boldsymbol{\theta}\|^2 \quad (3a)$$

$$= \boldsymbol{\theta}^\top \mathbf{J}^\top (\text{diag}(\mathbf{P}\mathbf{1}_{n_y}) \otimes \mathbf{I}_d) \mathbf{J} \boldsymbol{\theta} - 2\boldsymbol{\theta}^\top \mathbf{J}^\top (\mathbf{P} \otimes \mathbf{I}_d) \mathbf{y} + \mathbf{1}_{n_x}^\top \mathbf{P} \tilde{\mathbf{y}} \quad (3b)$$

$$s.t. \mathbf{P}\mathbf{1}_{n_y} \leq \mathbf{1}_{n_x}, \mathbf{1}_{n_x}^\top \mathbf{P} \leq \mathbf{1}_{n_y}^\top, \mathbf{1}_{n_x}^\top \mathbf{P} \mathbf{1}_{n_y} = n_p, \mathbf{P} \geq 0, \underline{\boldsymbol{\theta}} \leq \boldsymbol{\theta} \leq \bar{\boldsymbol{\theta}} \quad (3c)$$

where

$\boldsymbol{\theta}$: parameters of the spatial transformation
 $\mathbf{T}(\mathbf{x}_i)\boldsymbol{\theta} = \mathbf{J}(\mathbf{x}_i)\boldsymbol{\theta}$.

$\mathbf{J}(\mathbf{x}_i)$: the Jacobian matrix at point \mathbf{x}_i .

\mathbf{I}_d : the $d \times d$ identity matrix.

$\mathbf{1}_{n_x}$: the n_x -dimensional vector of all ones.

\otimes : the Kronecker product.

$\mathbf{P} = \{p_{ij}\}$: assignment matrix, with element $p_{ij}=1$ or 0 indicating that \mathbf{x}_i matches \mathbf{y}_j or not.

$\mathbf{1}_{n_x}^\top \mathbf{P} \mathbf{1}_{n_y} = n_p$: the number of matches is a priori known to be a constant integer n_p .

$\underline{\boldsymbol{\theta}}$ (resp. $\bar{\boldsymbol{\theta}}$): the lower (resp. upper) bound of $\boldsymbol{\theta}$.

$\mathbf{y} \triangleq [\mathbf{y}_1^\top, \dots, \mathbf{y}_{n_y}^\top]^\top$: a vector.

$\tilde{\mathbf{y}} \triangleq [\|\mathbf{y}_1\|_2^2, \dots, \|\mathbf{y}_{n_y}\|_2^2]^\top$: a vector.

$\mathbf{J} \triangleq [\mathbf{J}^\top(\mathbf{x}_1), \dots, \mathbf{J}^\top(\mathbf{x}_{n_x})]^\top$: a matrix.

For ease of derivation in the sequel, we need to convert matrix \mathbf{P} into a vector \mathbf{p} . Accordingly, the objective function takes

the following form [3]:

$$E(\mathbf{p}, \boldsymbol{\theta}) = \boldsymbol{\theta}^\top \text{mat}(\mathbf{B}\mathbf{p})\boldsymbol{\theta} - 2\boldsymbol{\theta}^\top \mathbf{A}\mathbf{p} + \boldsymbol{\rho}^\top \mathbf{p} \quad (4)$$

where

$$\begin{aligned} \mathbf{p} &\triangleq \text{vec}(\mathbf{P}): && \text{a vector.} \\ \boldsymbol{\rho} &\triangleq \mathbf{1}_{n_x} \otimes \bar{\mathbf{y}}: && \text{a vector.} \\ \mathbf{A} &\triangleq (\mathbf{J}^\top \otimes \mathbf{y}^\top) \mathbf{W}_{n_d}^{n_x n_y}: && \text{a matrix.} \\ \mathbf{B} &\triangleq (\mathbf{J}_2^\top \otimes \mathbf{I}_{n_\theta}) \mathbf{W}_{n_\theta}^{n_x, 1} (\mathbf{I}_{n_x} \otimes \mathbf{I}_{n_y}^\top): && \text{a matrix.} \\ \mathbf{J}_2 &\triangleq \left[\mathbf{J}(\mathbf{x}_1)^\top \mathbf{J}(\mathbf{x}_1), \dots, \mathbf{J}(\mathbf{x}_{n_x})^\top \mathbf{J}(\mathbf{x}_{n_x}) \right]^\top: && \text{a matrix.} \\ \mathbf{W}_d^{m,n} &\triangleq \mathbf{I}_m \otimes \left[\mathbf{I}_n \otimes (\mathbf{e}_d^1)^\top, \dots, \mathbf{I}_n \otimes (\mathbf{e}_d^d)^\top \right]^\top: && \text{a matrix.} \\ \text{vec}(\cdot): &&& \text{vectorization of a matrix by concatenating rows.} \\ n_\theta: &&& \text{the dimensionality of } \boldsymbol{\theta}. \\ \mathbf{e}_d^i: &&& \text{the } d\text{-dimensional column vector with only} \\ &&& \text{one nonzero unit element at the } i\text{-th position.} \\ \text{mat}(\cdot): &&& \text{reconstructs a matrix from a vector, which is} \\ &&& \text{the inverse of the operator } \text{vec}(\cdot). \end{aligned}$$

Since $\mathbf{1}_{n_x n_y}^\top \mathbf{p} = n_p$, a constant, for rows of \mathbf{B} containing identical elements, the result of them multiplied by \mathbf{p} can be replaced by constants. Also, redundant rows can be removed. Since $\text{mat}(\mathbf{B}\mathbf{p})$ is a symmetric matrix, \mathbf{B} surely contains redundant rows. Based on the above analysis, we therefore denote \mathbf{B}_2 as the matrix formed as a result of \mathbf{B} removing such rows. (Please refer to Sec. 6 and 7 for examples of \mathbf{B}_2). Consequently, E can be rewritten as [6]

$$E(\mathbf{p}, \boldsymbol{\theta}) = \boldsymbol{\theta}^\top [\text{mat}(\mathbf{K}\mathbf{B}_2\mathbf{p}) + \mathbf{C}] \boldsymbol{\theta} - 2\boldsymbol{\theta}^\top \mathbf{A}\mathbf{p} + \boldsymbol{\rho}^\top \mathbf{p} \quad (5)$$

where the nonzero elements of the constant matrix \mathbf{C} correspond to the rows of \mathbf{B} containing identical elements. The elements of the constant matrix \mathbf{K} take values in $\{0, 1\}$ and record the correspondences between the rows of \mathbf{B}_2 and those of \mathbf{B} .

5. Optimization

In this section, we begin by applying the bilinear relaxation formula, introduced in Section 3, to derive a lower bound function for our objective. This lower bound function's optimization can then be divided into separate optimizations over $\boldsymbol{\theta}$ and \mathbf{p} (discussed in Section 5.1). Subsequently, we demonstrate that it suffices to branch solely over $\boldsymbol{\theta}$ (explained in Section 5.2) and introduce a more effective method for computing the upper bound (outlined in Section 5.4). Lastly, we introduce the BnB algorithm (presented in Section 5.5), which offers global optimization for the objective function.

5.1. Lower bound function derivation

We derive a lower bound function of $E(\mathbf{p}, \boldsymbol{\theta})$ via variable substitution and bilinear relaxation, as illustrated in Fig. 2. In the following, we explain each step of the approach in detail.

By introducing new variables $\boldsymbol{\Theta} \triangleq \boldsymbol{\theta}\boldsymbol{\theta}^\top$, $\boldsymbol{\Gamma} \triangleq \text{mat}(\mathbf{K}\mathbf{B}_2\mathbf{p})$ and $\boldsymbol{\eta} \triangleq -2\mathbf{A}\mathbf{p}$, we can rewrite the above objective function as a quadratic function:

$$E(\mathbf{p}, \boldsymbol{\theta}, \boldsymbol{\Theta}, \boldsymbol{\Gamma}, \boldsymbol{\eta}) = \text{trace}(\boldsymbol{\Gamma}\boldsymbol{\Theta}) + \boldsymbol{\theta}^\top \mathbf{C}\boldsymbol{\theta} + \boldsymbol{\theta}^\top \boldsymbol{\eta} + \boldsymbol{\rho}^\top \mathbf{p} \quad (6)$$

We note that E contains bilinear terms $\text{trace}(\boldsymbol{\Gamma}\boldsymbol{\Theta})$ and $\boldsymbol{\theta}^\top \boldsymbol{\eta}$, which interconnect $\boldsymbol{\Gamma}$ and $\boldsymbol{\Theta}$ (resp. $\boldsymbol{\theta}$ and $\boldsymbol{\eta}$), making optimization challenging. To tackle this challenge, we use the bilinear relaxation formula introduced in Section 3 to relax these terms into linear ones. The first relaxation is:

$$\begin{aligned} &\text{trace}(\boldsymbol{\Gamma}\boldsymbol{\Theta}) \\ &\text{bilinear} \downarrow \text{relaxation} \\ &\text{trace}(\mathbf{H}^0 \boldsymbol{\Theta}) + \text{trace}(\mathbf{H}^1 \boldsymbol{\Gamma}) + \text{trace}(\mathbf{H}^2 \mathbf{1}\mathbf{1}^\top) \end{aligned} \quad (7)$$

where in accordance with equations (1) and (2), the coefficients can be calculated as

$$\mathbf{H}^0 = \frac{\underline{\boldsymbol{\Gamma}} + \bar{\boldsymbol{\Gamma}}}{2}, \mathbf{H}^1 = \frac{\underline{\boldsymbol{\Theta}} + \bar{\boldsymbol{\Theta}}}{2}, \mathbf{H}^2 = -\frac{\underline{\boldsymbol{\Gamma}\boldsymbol{\Theta}} + \bar{\boldsymbol{\Gamma}\boldsymbol{\Theta}}}{2} \quad (8)$$

Here we use underline (resp. overline) to denote the lower (resp. upper) bounds of matrices $\boldsymbol{\Theta}$ and $\boldsymbol{\Gamma}$. It is also worth noting that the range $[\underline{\boldsymbol{\Theta}}, \bar{\boldsymbol{\Theta}}]$ of $\boldsymbol{\Theta}$ can be derived from the range $[\underline{\boldsymbol{\theta}}, \bar{\boldsymbol{\theta}}]$ of $\boldsymbol{\theta}$ based on relation $\boldsymbol{\Theta} = \boldsymbol{\theta}\boldsymbol{\theta}^\top$, as explained in Section 5.3.

The second relaxation is:

$$\begin{aligned} &\boldsymbol{\theta}^\top \boldsymbol{\eta} \\ &\text{bilinear} \downarrow \text{relaxation} \\ &(\mathbf{g}^0)^\top \boldsymbol{\theta} + (\mathbf{g}^1)^\top \boldsymbol{\eta} + \mathbf{1}_{n_\theta}^\top \mathbf{g}^2 \end{aligned} \quad (9)$$

where in accordance with equations (1) and (2), the coefficients can be calculated as

$$\mathbf{g}^0 = \frac{\underline{\boldsymbol{\eta}} + \bar{\boldsymbol{\eta}}}{2}, \mathbf{g}^1 = \frac{\underline{\boldsymbol{\theta}} + \bar{\boldsymbol{\theta}}}{2}, \mathbf{g}^2 = \frac{\underline{\boldsymbol{\eta}\boldsymbol{\theta}} + \bar{\boldsymbol{\eta}\boldsymbol{\theta}}}{2} \quad (10)$$

Here, the underline and overline have the same meaning as before.

Taking into account the above relaxations, we get the following lower bound function:

$$\begin{aligned} E_l(\mathbf{p}, \boldsymbol{\theta}, \boldsymbol{\Theta}, \boldsymbol{\Gamma}, \boldsymbol{\eta}) = &\text{trace}(\mathbf{H}^0 \boldsymbol{\Theta}) + \text{trace}(\mathbf{H}^1 \boldsymbol{\Gamma}) + \text{trace}(\mathbf{H}^2 \mathbf{1}\mathbf{1}^\top) \\ &+ \boldsymbol{\theta}^\top \mathbf{C}\boldsymbol{\theta} + \boldsymbol{\theta}^\top \mathbf{g}^0 + (\mathbf{g}^1)^\top \boldsymbol{\eta} + \mathbf{1}^\top \mathbf{g}^2 + \boldsymbol{\rho}^\top \mathbf{p} \end{aligned} \quad (11)$$

By substituting back $\boldsymbol{\theta}\boldsymbol{\theta}^\top \leftarrow \boldsymbol{\Theta}$, $\text{mat}(\mathbf{K}\mathbf{B}_2\mathbf{p}) \leftarrow \boldsymbol{\Gamma}$ and $-2\mathbf{A}\mathbf{p} \leftarrow \boldsymbol{\eta}$, we get the final form of the lower bound function:

$$\begin{aligned} E_l(\mathbf{p}, \boldsymbol{\theta}) = &\boldsymbol{\theta}^\top \mathbf{H}^0 \boldsymbol{\theta} + \text{trace}(\mathbf{H}^1 \text{mat}(\mathbf{K}\mathbf{B}_2\mathbf{p})) + \text{trace}(\mathbf{H}^2 \mathbf{1}\mathbf{1}^\top) \\ &+ \boldsymbol{\theta}^\top \mathbf{C}\boldsymbol{\theta} + \boldsymbol{\theta}^\top \mathbf{g}^0 + (\mathbf{g}^1)^\top (-2\mathbf{A}\mathbf{p}) + \mathbf{1}_{n_\theta}^\top \mathbf{g}^2 + \boldsymbol{\rho}^\top \mathbf{p} \end{aligned} \quad (12)$$

It is apparent that the minimization of E_l under constraints (3c) can be decomposed into separate optimizations over \mathbf{p} and $\boldsymbol{\theta}$.

The optimization over \mathbf{p} is

$$\min_{\mathbf{p}} \text{trace}(\mathbf{H}^1 \text{mat}(\mathbf{K}\mathbf{B}_2\mathbf{p})) + (\mathbf{g}^1)^\top (-2\mathbf{A}\mathbf{p}) + \boldsymbol{\rho}^\top \mathbf{p} \quad (13a)$$

$$\text{s.t. } \mathbf{p} \in \Omega \quad (13b)$$

$$\begin{aligned}
E(\mathbf{p}, \boldsymbol{\theta}) &= \theta^\top \text{mat}(\mathbf{KB}_2\mathbf{p})\boldsymbol{\theta} & + \boldsymbol{\theta}^\top \mathbf{C}\boldsymbol{\theta} & - 2\boldsymbol{\theta}^\top \mathbf{A}\mathbf{p} & + \boldsymbol{\rho}^\top \mathbf{p} \\
&\quad \text{define } \boldsymbol{\Theta} \triangleq \boldsymbol{\theta}\boldsymbol{\theta}^\top \downarrow \Gamma \triangleq \text{mat}(\mathbf{KB}_2\mathbf{p}) & & \text{define } \boldsymbol{\eta} \triangleq -2\mathbf{A}\mathbf{p} & \\
E(\mathbf{p}, \boldsymbol{\theta}, \boldsymbol{\Theta}, \boldsymbol{\Gamma}, \boldsymbol{\eta}) &= \text{trace}(\boldsymbol{\Gamma}\boldsymbol{\Theta}) & + \boldsymbol{\theta}^\top \mathbf{C}\boldsymbol{\theta} & + \boldsymbol{\theta}^\top \boldsymbol{\eta} & + \boldsymbol{\rho}^\top \mathbf{p} \\
&\quad \text{bilinear} \downarrow \text{relaxation} & & \text{bilinear} \downarrow \text{relaxation} & \\
E_l(\mathbf{p}, \boldsymbol{\theta}, \boldsymbol{\Theta}, \boldsymbol{\Gamma}, \boldsymbol{\eta}) &= \text{trace}(\mathbf{H}^0\boldsymbol{\Theta}) + \text{trace}(\mathbf{H}^1\boldsymbol{\Gamma}) + \text{trace}(\mathbf{H}^2\mathbf{1}\mathbf{1}^\top) & + \boldsymbol{\theta}^\top \mathbf{C}\boldsymbol{\theta} & + (\mathbf{g}^0)^\top \boldsymbol{\theta} + (\mathbf{g}^1)^\top \boldsymbol{\eta} + \mathbf{1}_{n_0}^\top \mathbf{g}^2 & + \boldsymbol{\rho}^\top \mathbf{p} \\
&\quad \text{substitute back } \boldsymbol{\theta}\boldsymbol{\theta}^\top \Leftarrow \boldsymbol{\Theta} \downarrow \text{mat}(\mathbf{KB}_2\mathbf{p}) \Leftarrow \boldsymbol{\Gamma} & & \text{substitute back } \downarrow -2\mathbf{A}\mathbf{p} \Leftarrow \boldsymbol{\eta} & \\
E_l(\mathbf{p}, \boldsymbol{\theta}) &= \boldsymbol{\theta}^\top \mathbf{H}^0 \boldsymbol{\theta} + \text{trace}(\mathbf{H}^1 \text{mat}(\mathbf{KB}_2\mathbf{p})) + \text{trace}(\mathbf{H}^2 \mathbf{1}\mathbf{1}^\top) & + \boldsymbol{\theta}^\top \mathbf{C}\boldsymbol{\theta} & + (\mathbf{g}^0)^\top \boldsymbol{\theta} + (\mathbf{g}^1)^\top (-2\mathbf{A}\mathbf{p}) + \mathbf{1}_{n_0}^\top \mathbf{g}^2 & + \boldsymbol{\rho}^\top \mathbf{p}
\end{aligned}$$

Figure 2: Derivation of a lower bound function $E_l(\mathbf{p}, \boldsymbol{\theta})$ of $E(\mathbf{p}, \boldsymbol{\theta})$ via variable substitution and bilinear relaxation.

where Ω denotes the feasible region of \mathbf{p} as defined in (3c). This is an n_p -cardinality linear assignment problem and can be transformed into a standard linear assignment problem [39] and then efficiently solved by combinatorial optimization algorithms such as LAPJV [40].

The optimization over $\boldsymbol{\theta}$ is:

$$\min_{\boldsymbol{\theta}} \boldsymbol{\theta}^\top (\mathbf{H}^0 + \mathbf{C})\boldsymbol{\theta} + \boldsymbol{\theta}^\top \mathbf{g}^0 \quad (14a)$$

$$s.t. \underline{\boldsymbol{\theta}} \leq \boldsymbol{\theta} \leq \bar{\boldsymbol{\theta}} \quad (14b)$$

In the next section, we will delve into the solution for this problem.

5.2. Branching strategy

According to the result stated in Section 3, for the bilinear term $\boldsymbol{\theta}^\top \boldsymbol{\eta}$, for its linear lower bound function to converge to it, it suffices to branch over $\boldsymbol{\theta}$ and leave the range of $\boldsymbol{\eta}$ fixed. Here, utilizing $\boldsymbol{\eta} = -2\mathbf{A}\mathbf{p}$, the fixed range $[\underline{\boldsymbol{\eta}}, \bar{\boldsymbol{\eta}}]$ of $\boldsymbol{\eta}$ can be computed as

$$\underline{\eta}_i = \min_{\mathbf{p} \in \Omega} (-2\mathbf{A}\mathbf{p})_i \quad (15)$$

$$\bar{\eta}_i = \max_{\mathbf{p} \in \Omega} (-2\mathbf{A}\mathbf{p})_i \quad (16)$$

Likewise, for the bilinear term $\text{trace}(\boldsymbol{\Gamma}\boldsymbol{\Theta})$, for its linear lower bound function to converge to it, we only need to branch over $\boldsymbol{\theta}$ (since the range of $\boldsymbol{\theta}$ determines the range of $\boldsymbol{\Theta}$ as explained in Sec. 5.3) and leave the range of $\boldsymbol{\Gamma}$ fixed. Here, utilizing $\boldsymbol{\Gamma} = \text{mat}(\mathbf{KB}_2\mathbf{p})$, the fixed range $[\underline{\boldsymbol{\Gamma}}, \bar{\boldsymbol{\Gamma}}]$ of $\boldsymbol{\Gamma}$ can be computed as follows:

$$\underline{\Gamma}_{ij} = \min_{\mathbf{p} \in \Omega} [\text{mat}(\mathbf{KB}_2\mathbf{p})]_{ij} \quad (17)$$

$$\bar{\Gamma}_{ij} = \max_{\mathbf{p} \in \Omega} [\text{mat}(\mathbf{KB}_2\mathbf{p})]_{ij} \quad (18)$$

With this choice of $\underline{\boldsymbol{\Gamma}}$ and $\bar{\boldsymbol{\Gamma}}$, it has been empirically demonstrated that

$$\mathbf{H}^0 + \mathbf{C} = \frac{(\underline{\boldsymbol{\Gamma}} + \mathbf{C}) + (\bar{\boldsymbol{\Gamma}} + \mathbf{C})}{2} \geq 0 \quad (19)$$

Please refer to Section 5.6 for relevant experiments and Appendix for a weaker assertion. This result implies that problem

(14a) (14b) is now a convex quadratic program. Consequently, utilizing solvers for convex quadratic programs, such as MATLAB's quadprog function, guarantees global optimality. We will address the proof of (19) in our future research.

We also note that (15), (16), (17) and (18) are n_p -cardinality linear assignment problems, which can be efficiently solved by the aforementioned algorithms.

In conclusion, in our BnB algorithm, we only need to branch over $\boldsymbol{\theta}$. Therefore, the dimension of the branching space of our BnB algorithm is low and the proposed algorithm can converge quickly.

5.3. The range of $\boldsymbol{\Theta}$ from the range of $\boldsymbol{\theta}$

Given the relationship $\boldsymbol{\Theta} = \boldsymbol{\theta}\boldsymbol{\theta}^\top$, and the specified range $[\underline{\boldsymbol{\theta}}, \bar{\boldsymbol{\theta}}]$ of $\boldsymbol{\theta}$, we can determine the range $[\underline{\boldsymbol{\Theta}}, \bar{\boldsymbol{\Theta}}]$ of $\boldsymbol{\Theta}$ as follows:

$$[\underline{\Theta}_{ij}, \bar{\Theta}_{ij}] = \begin{cases} [\underline{\theta}_i, \bar{\theta}_i] \cdot [\underline{\theta}_j, \bar{\theta}_j], & \text{if } i \neq j \\ [\underline{\theta}_i, \bar{\theta}_i]^2, & \text{if } i = j \end{cases}$$

Here, employing interval arithmetic, the product operator is defined as:

$$[\underline{\theta}_i, \bar{\theta}_i] \cdot [\underline{\theta}_j, \bar{\theta}_j] = [\min(\underline{\theta}_i \underline{\theta}_j, \underline{\theta}_i \bar{\theta}_j, \bar{\theta}_i \underline{\theta}_j, \bar{\theta}_i \bar{\theta}_j), \max(\underline{\theta}_i \underline{\theta}_j, \underline{\theta}_i \bar{\theta}_j, \bar{\theta}_i \underline{\theta}_j, \bar{\theta}_i \bar{\theta}_j)]$$

Additionally, the square operator is defined as:

$$[\underline{\theta}_i, \bar{\theta}_i]^2 = \begin{cases} [\min(\underline{\theta}_i^2, \bar{\theta}_i^2), \max(\underline{\theta}_i^2, \bar{\theta}_i^2)], & \text{if } 0 \notin [\underline{\theta}_i, \bar{\theta}_i] \\ [0, \max(\underline{\theta}_i^2, \bar{\theta}_i^2)], & \text{if } 0 \in [\underline{\theta}_i, \bar{\theta}_i] \end{cases}$$

5.4. Upper bound

When we substitute the solutions for \mathbf{p} and $\boldsymbol{\theta}$ obtained during the computation of the lower bound into $E(\mathbf{p}, \boldsymbol{\theta})$, we can derive an upper bound. However, the solution for $\boldsymbol{\theta}$ obtained in this process might significantly differ from the optimal $\boldsymbol{\theta}$, especially in the early iterations of the BnB algorithm. This discrepancy can lead to a poor computed upper bound.

To address this issue, we can rewrite the objective function $E(\mathbf{p}, \boldsymbol{\theta})$ as a function of \mathbf{p} alone by eliminating $\boldsymbol{\theta}$, based on a result from [6]:

$$E(\mathbf{p}) = -\mathbf{p}^\top \mathbf{A}^\top [\text{mat}(\mathbf{KB}_2\mathbf{p}) + \mathbf{C}]^{-1} \mathbf{A}\mathbf{p} + \boldsymbol{\rho}^\top \mathbf{p}. \quad (20)$$

Therefore, by substituting the computed \mathbf{p} into this function, we obtain a value for E , which serves as an upper bound.

5.5. Branch-and-Bound

Based on the aforementioned preparations, we are now poised to apply the BnB algorithm to optimize E . To initiate the process, we utilize the initial range of θ to form the initial hypercube M . Subsequently, during each iteration of the algorithm, we identify the hypercube that yields the lowest lower bound among all available hypercubes. This selected hypercube is then further subdivided to enhance the global lower bound of the problem. Simultaneously, the upper bound is refined by assessing $E(\mathbf{p})$ using solutions generated during the computation of the lower bounds. For a comprehensive overview, refer to Algorithm 1.

Algorithm 1: A BnB algorithm for minimizing E

- 1 Set tolerance error $\epsilon > 0$ and initial hypercube M . Let $\mathcal{M}_1 = \mathcal{N}_1 = \{M\}$ where \mathcal{M}_k and \mathcal{N}_k denote the collection of all hypercubes and the collection of active hypercubes at iteration k , respectively.
 - 2 **for** $k = 1, 2, \dots$ **do**
 - 3 For each hypercube $M \in \mathcal{N}_k$, minimize the lower bound function E_l to obtain the optimal point correspondence solution $\mathbf{p}(M)$ and the optimal value $\beta(M)$. $\beta(M)$ is a lower bound for M .
 - 4 Let \mathbf{p}^k be the best among all feasible solutions so far encountered: \mathbf{p}^{k-1} and all $\mathbf{p}(M)$ for $M \in \mathcal{N}_k$. Delete all $M \in \mathcal{M}_k$ such that $\beta(M) \geq E(\mathbf{p}^k) - \epsilon$. Let \mathcal{R}_k be the remaining collection of hypercubes.
 - 5 If $\mathcal{R}_k = \emptyset$, terminate: \mathbf{p}^k is the global ϵ -minimum solution.
 - 6 Select the hypercube M yielding the lowest lower bound and divide it into two sub-hypercubes M_1, M_2 by bisecting the longest edge.
 - 7 Let $\mathcal{N}_{k+1} = \{M_1, M_2\}$ and $\mathcal{M}_{k+1} = (\mathcal{R}_k \setminus M) \cup \mathcal{N}_{k+1}$.
 - 8 **end**
-

5.6. Positive semidefiniteness of $\mathbf{H}^0 + \mathbf{C}$

To confirm the assertion that $\mathbf{H}^0 + \mathbf{C} \geq 0$, we utilize the separate outliers and inliers test detailed in Section 8.1.1, with an outlier to data ratio set at 0.3. We present histograms of the smallest eigenvalues of the matrix $\mathbf{H}^0 + \mathbf{C}$ across 100 registration instances in Figure 3. The result consistently support the claim that $\mathbf{H}^0 + \mathbf{C} \geq 0$, underscoring the efficacy of the proposed algorithm.

5.7. Convergence of the BnB algorithm

To assess the convergence of the proposed BnB algorithm, we conducted the separate outliers and inliers test detailed in Sec. 8.1.1, with an outlier to data ratio set at 0.3. The experimental results are depicted in Fig. 4. Key observations include: 1) A narrower initial range of θ results in a tighter duality gap, evidenced by improved upper and lower bounds. This suggests that leveraging additional information about the range of θ could effectively reduce the duality gap in practical applications. 2) Easier problem instances, such as the fish test

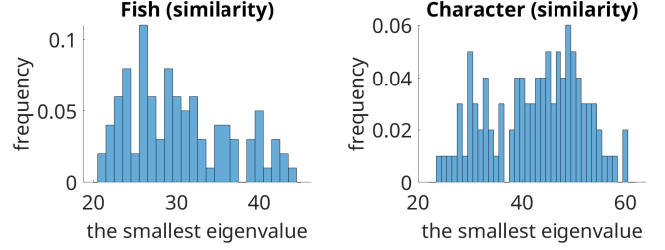


Figure 3: Histograms depicting the smallest eigenvalue of $\mathbf{H}^0 + \mathbf{C}$ across 100 registration instances.

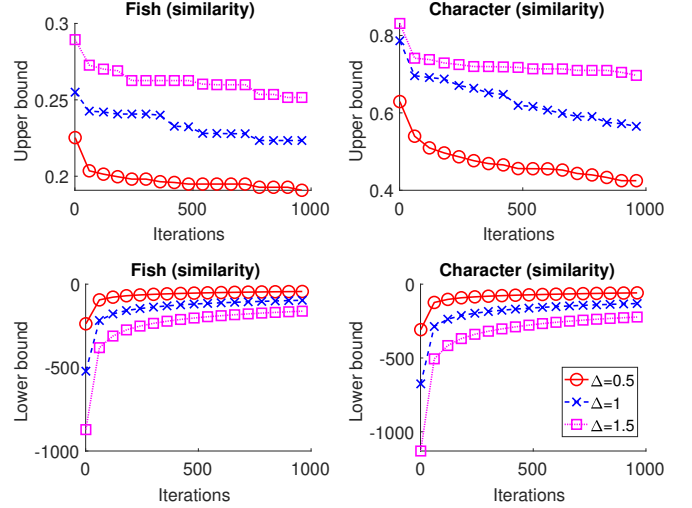


Figure 4: Upper (first row) and lower bounds (second row) generated in each iteration of RPM-BP. Our method is tested with the n_p value chosen as the ground truth and with varying initial ranges of θ : $[\theta_{gt} - \Delta, \theta_{gt} + \Delta]$, where θ_{gt} represents the ground truth θ solution. Here, the margin Δ takes values of 0.5, 1, and 1.5 respectively.

compared to the character test, exhibit a tighter duality gap, thus leads to faster convergence.

Properties 2) suggests that employing a fixed duality gap threshold as the stopping criterion for all types of problems may not be a good idea. It may happen that a threshold is set too small for challenging problems, leading to prolonged execution times. Conversely, it might be set too large for simpler problems, resulting in premature termination. Therefore, following [6], we adopt the maximum branching depth as our stopping criterion.

6. Application 1: 2D similarity/affine registration

Our algorithm can handle 2D similarity and affine transformations since both of them can be written as the form of $T(\mathbf{x}|\theta) = J(\mathbf{x})\theta$. A 2D similarity transformation has the form

$$T(\mathbf{x}|\theta) = \begin{bmatrix} \theta_1 & -\theta_2 \\ \theta_2 & \theta_1 \end{bmatrix} \begin{bmatrix} x^1 \\ x^2 \end{bmatrix} + \begin{bmatrix} \theta_3 \\ \theta_4 \end{bmatrix} = \begin{bmatrix} x^1 & -x^2 & 1 & 0 \\ x^2 & x^1 & 0 & 1 \end{bmatrix} \theta$$

where $[\theta_3, \theta_4]^T$ is translation and $\theta_1 = s \cos(\phi)$ and $\theta_2 = s \sin(\phi)$ with s being scale and ϕ being rotation angle. It can be derived that $\mathbf{B}_2 = \mathbf{B}([1, 3, 4], :)$ and $\mathbf{C} = \text{diag}([0, 0, n_p, n_p])$.

A 2D affine transformation has the form

$$T(\mathbf{x}|\boldsymbol{\theta}) = \begin{bmatrix} \theta_1 & \theta_2 \\ \theta_3 & \theta_4 \end{bmatrix} \begin{bmatrix} x^1 \\ x^2 \end{bmatrix} + \begin{bmatrix} \theta_5 \\ \theta_6 \end{bmatrix} = \begin{bmatrix} x^1 & x^2 & 0 & 0 & 1 & 0 \\ 0 & 0 & x^1 & x^2 & 0 & 1 \end{bmatrix} \boldsymbol{\theta}$$

It can be derived that $\mathbf{B}_2 = \mathbf{B}([1, 2, 5, 8, 11], :)$ and $\mathbf{C} = \text{diag}([0, 0, 0, 0, n_p, n_p])$.

7. Application 2: 3D rigid registration

Theoretically, our method can handle 3D affine transformation since it takes the form $T(\mathbf{x}|\boldsymbol{\theta}) = J(\mathbf{x})\boldsymbol{\theta}$. A 2D affine transformation has the form

$$T(\mathbf{x}|\boldsymbol{\theta}) = \begin{bmatrix} \theta_1 & \theta_2 & \theta_3 \\ \theta_4 & \theta_5 & \theta_6 \\ \theta_7 & \theta_8 & \theta_9 \end{bmatrix} \begin{bmatrix} x^1 \\ x^2 \\ x^3 \end{bmatrix} + \begin{bmatrix} \theta_{10} \\ \theta_{11} \\ \theta_{12} \end{bmatrix} \\ = \begin{bmatrix} x^1 & x^2 & x^3 & 0 & 0 & 0 & 0 & 0 & 0 & 1 & 0 & 0 \\ 0 & 0 & 0 & x^1 & x^2 & x^3 & 0 & 0 & 0 & 0 & 1 & 0 \\ 0 & 0 & 0 & 0 & 0 & 0 & x^1 & x^2 & x^3 & 0 & 0 & 1 \end{bmatrix} \boldsymbol{\theta}$$

It can be derived that $\mathbf{B}_2 = \mathbf{B}([1, 2, 3, 10, 14, 15, 22, 27, 34], :)$ and $\mathbf{C} = \text{diag}(\underbrace{[0, \dots, 0]_{9 \text{ zeros}}, n_p, n_p, n_p})$. Nevertheless, the 3D affine transformation has many parameters, causing our method to converge slowly. Therefore, for the 3D case, we instead focus on rigid transformation instead.

Using the angle-axis representation, a 3D rotation can be represented as a 3D vector \mathbf{r} , with axis $\mathbf{r}/\|\mathbf{r}\|$ and angle $\|\mathbf{r}\|$. The corresponding 3×3 rotation matrix $\mathbf{R} \in \mathbb{S}\mathbb{O}_3$ for \mathbf{r} can be obtained using matrix exponential map as [20]

$$\mathbf{R} = \mathbf{I}_3 + \frac{[\mathbf{r}]_{\times} \sin \|\mathbf{r}\|}{\|\mathbf{r}\|} + \frac{[\mathbf{r}]_{\times}^2 (1 - \cos \|\mathbf{r}\|)}{\|\mathbf{r}\|^2} \quad (21)$$

where $[\cdot]_{\times}$ denotes the skew-symmetric matrix representation:

$$[\mathbf{r}]_{\times} = \begin{bmatrix} 0 & -r_3 & r_2 \\ r_3 & 0 & -r_1 \\ -r_2 & r_1 & 0 \end{bmatrix} \quad (22)$$

where r_i is the i -th element of \mathbf{r} .

3D rigid transformation is a special case of 3D affine transformation, whereas our method is capable of handling 3D affine transformation. Therefore, we aim to adapt our method from Section 5 to accommodate 3D rigid transformation as well. Here's the procedure: We continue to use the algorithm outlined in Section 5 for registration, where the transformation is defined as a 3D affine transformation: $T(\mathbf{x}|\mathbf{R}, \mathbf{t}) = \mathbf{R}\mathbf{x} + \mathbf{t}$, with \mathbf{R} representing the linear part of the affine transformation. The main differences from the algorithm in Section 5 are as follows: (1) Instead of branching over \mathbf{R} and \mathbf{t} , we branch over \mathbf{r} and \mathbf{t} . (2) In each iteration of the BnB algorithm, given the range of \mathbf{r} , we calculate the range of \mathbf{R} from the range of \mathbf{r} based on equation (21). (The method for efficiently computing the range of \mathbf{R} is discussed in Section 7.1.)

In the above algorithm, (20) is employed to compute the upper bound, assuming that the transformation can be affine. While methods exist (see Sec. 5.3 of [6]) for computing the

upper bound with a rigid transformation constraint, they often result in higher upper bounds, which slows down our method's convergence. Hence, we opt to use (20) for computing the upper bound in this work.

7.1. The range of \mathbf{R} from the range of \mathbf{r}

Given a range $[\underline{\mathbf{r}}, \bar{\mathbf{r}}]$ for \mathbf{r} , the computation of the range of \mathbf{R} , as derived from (21), involves determining R_{ij} values within the bounds specified by $\underline{\mathbf{r}}$ and $\bar{\mathbf{r}}$. This computation can be facilitated through optimization solvers such as the Matlab function *fmincon*. However, this process can be burdensome, particularly when executed iteratively as a subroutine of the Branch and Bound (BnB) algorithm. In order to alleviate this computational burden, we propose the utilization of precomputation techniques to enhance efficiency. Specifically, prior to initiating the BnB algorithm, we construct a regular grid, with a predefined width (set as 150 in this study), over the initial cube $[\underline{\mathbf{r}}_0, \bar{\mathbf{r}}_0]$. Subsequently, we compute the corresponding R_{ij} values for all grid points and store them. During the execution of the BnB algorithm, when presented with a range $[\underline{\mathbf{r}}, \bar{\mathbf{r}}]$, we first identify the grid points falling within this range. Subsequently, we determine the minimum and maximum pre-computed R_{ij} values for these points, effectively approximating $\min\{R_{ij}|\underline{\mathbf{r}} \leq \mathbf{r} \leq \bar{\mathbf{r}}\}$ and $\max\{R_{ij}|\underline{\mathbf{r}} \leq \mathbf{r} \leq \bar{\mathbf{r}}\}$.

8. Experiments

We implement the proposed algorithm, referred to as RPM-BP, using Matlab R2023b. To evaluate its performance, we conduct comparisons with other methods on a computer equipped with 6-core CPUs running at 3.2 GHz.

For the competing methods that solely produce point correspondences, we utilize the generated point correspondences to compute the optimal affine transformation between two sets of points. The matching error is then quantified as the root-mean-square distance between the transformed model inliers and their corresponding scene inliers.

To ensure efficient computation, we set the maximum branching depth of RPM-BP to 12.

8.1. 2D registration

We conduct comparisons with RPM-HTB [6], RPM-PA [5] and RPM-CAV [4], all of which utilize global optimization techniques. These methods are adept at handling partial overlap and permit arbitrary similarity transformations between two point sets, rendering them suitable candidates for our comparative analysis.

8.1.1. 2D synthetic data

Synthetic data offer a convenient means to assess specific facets of an algorithm's performance. We conduct five distinct types of tests to gauge a method's resilience to various disturbances:

i) Deformation test: The prototype shape undergoes non-rigid deformation to generate the scene set.

ii) Noise test: Positional noise is introduced to perturb the prototype shape, resulting in the scene point set.

iii) Mixed outliers and inliers test: Random outliers are superimposed on the prototype shape to create both point sets.

iv) Separate outliers and inliers test: Random outliers are added to different areas of the prototype shape, generating the two point sets.

v) Occlusion+outlier test: Initially, the prototype shape is occluded to produce the two point sets. Subsequently, random outliers (with a fixed outlier-to-data ratio of 0.5) are incorporated into different regions of the point sets.

These tests are visually illustrated in Fig. 5. Additionally, to assess a method’s capability in handling arbitrary rotation and scaling, random rotations and scalings within the range of [0.5, 1.5] are applied when generating the two point sets. Fig. 7 provides examples of registrations performed by different methods.

The registration errors produced by various methods are depicted in the top two rows of Fig. 6. The result suggests that, in comparison to alternative methods, RPM-BP and RPM-HTB, with n_p chosen as the ground truth, exhibits robustness against deformation, noise, and outliers when the outliers are distinct from the inliers. However, their robustness diminishes when outliers are intermixed with inliers. This limitation arises due to the fact that our method lacks ϵ -global optimality, as discussed in Sec. 5.7, thereby affecting its robustness.

Regarding different transformation options, RPM-BP, when employing similarity transformation, demonstrates greater resilience to various disturbances than when utilizing affine transformation.

Furthermore, the choice of n_p value significantly influences the performance of RPM-BP. Specifically, RPM-BP with an n_p value close to the ground truth yields superior results. Moreover, RPM-BP displays less sensitivity to variations in the n_p value compared to RPM-HTB, particularly evident in tests involving outliers and occlusion.

The average run times for various methods are depicted in the bottom row of Fig. 6. RPM-BP exhibits the best performance in scenarios involving deformation, positional noise, and mixed inlier-outlier tests. Comparing different transformation options, RPM-BP employing similarity transformation proves to be more efficient than when employing affine transformation. This efficiency is attributed to the lesser number of parameters involved in similarity transformation.

The outlier tests also provide insights into how various methods scale with problem size. Among them, RPM-BP, RPM-HTB, and RPM-CAV demonstrate the best scalability, followed by RPM-PA.

8.2. 3D registration

8.2.1. 3D synthetic data

Similar to the experimental setup detailed in Sec. 8.1.1, we conducted five types of tests to assess a method’s resilience against various disturbances. These tests include: i) Deformation test, ii) Noise test, iii) Mixed outliers and inliers test, iv) Separate outliers and inliers test, and v) Occlusion+outlier

test. Refer to Fig. 8 for an illustration. Additionally, examples of registration by different methods are depicted in Fig. 10.

The top 2 rows of Fig. 9 displays registration errors from various methods. Results show that RPM-BP and RPM-HTB, with n_p chosen as the ground truth, exhibits robustness against deformation, noise, and outliers when outliers are separate from inliers. However, they loses robustness when outliers are mixed with inliers. In contrast, GORE and TEASER++ struggle with handling deformation, noise, and outliers, especially when outliers are mixed with inliers, likely due to their reliance on features. In terms of different choices of n_p , RPM-BP performs significantly better when n_p closely matches the ground truth.

The bottom row of Fig. 9 displays the average run times for various methods. TEASER++ emerges as the fastest, with Go-ICP following closely behind, and RPM-BP and RPM-HTB trailing after. GORE consistently exhibits slower performance across most cases. Notably, FRS experiences a rapid decline in efficiency when faced with challenging registration problems, such as an increase in outliers in both types of outlier tests.

Examining the two types of outlier tests also reveals how different methods scale with problem size. Go-ICP and GORE demonstrate the best scalability with problem size, followed by TEASER++, RPM-BP and RPM-HTB. Conversely, FRS exhibits the poorest scalability with problem size.

8.2.2. 3DMatch dataset

The 3DMatch benchmark [41] encompasses scans of 62 scenes sourced from five established RGB-D reconstruction datasets (sun3d, 7-scenes, rgb-d-scenes-v2, bundlefusion, and analysis-by-synthesis). D3Feat [42] offers a unified file structure and format. For convenience, we utilize the scan pairs provided by D3Feat to assess the performance of various methods.

The matching errors from different methods are depicted in Fig. 11. The results indicate that RPM-BP and RPM-HTB generally outperform Go-ICP and FRS but lag behind GORE and TEASER++. The superior performance of GORE and TEASER++ is partly attributed to their use of features, which significantly enhances their capability to match complex structures. In contrast, other methods rely solely on point position information. Additionally, the 3DMatch benchmark comprises purely rigid transformations, aligning well with the assumptions of GORE and TEASER++. Among RPM-BP and RPM-HTB, RPM-BP exhibits slightly superior performance, particularly evident in the sun3d and rgb-d-scenes-v2 tests.

Examples of registration by different methods are presented in Fig. 12.

9. Conclusion

In this paper, we introduced a BnB-based point set registration algorithm capable of aligning partially overlapping point sets while remaining invariant to the corresponding transformation. The method offers several advantages: the lower bound can be efficiently computed via linear assignment and low-dimensional convex quadratic program, and the dimensionality of the branching space matches the number of transformation

parameters. These attributes make the method computationally efficient and scalable with problem size. By employing the BnB algorithm, our method demonstrates robustness against non-rigid deformations, positional noise, and outliers, particularly when outliers are distinct from inliers compared to state-of-the-art approaches.

However, the proposed method is limited to transformations with few parameters due to the exponential complexity of the BnB algorithm with respect to the dimensionality of the branching space. Additionally, the method's robustness is significantly affected by the parameter setting for n_p . In the future, we plan to develop an adaptive scheme for setting n_p .

ACKNOWLEDGMENTS

This work was supported by the Fundamental Research Program of Shanxi Province (202103021223381, 202303021222267 and 202303021222271) and Science and Technological Innovation Program of Higher Education Institutions in Shanxi under Grant (2023L335)

References

- [1] H. Chui, A. Rangarajan, A new point matching algorithm for non-rigid registration, *Computer Vision and Image Understanding* 89 (2-3) (2003) 114–141.
- [2] W. Lian, L. Zhang, M.-H. Yang, An efficient globally optimal algorithm for asymmetric point matching, *IEEE Transactions on Pattern Analysis and Machine Intelligence* 39 (7) (2017) 1281–1293.
- [3] W. Lian, L. Zhang, Point matching in the presence of outliers in both point sets: A concave optimization approach, in: *IEEE Conference on Computer Vision and Pattern Recognition*, 2014, pp. 352–359.
- [4] W. Lian, L. Zhang, A concave optimization algorithm for matching partially overlapping point sets, *Pattern Recognition* 103 (2020) 107322. doi:<https://doi.org/10.1016/j.patcog.2020.107322>.
- [5] W. Lian, W. Zuo, Z. Cui, A polyhedral annexation algorithm for aligning partially overlapping point sets, *IEEE Access* 9 (2021) 166750–166761. doi:[10.1109/ACCESS.2021.3135863](https://doi.org/10.1109/ACCESS.2021.3135863).
- [6] W. Lian, W. Zuo, Hybrid trilinear and bilinear programming for aligning partially overlapping point sets, *Neurocomputing* 551 (2023) 126482. doi:<https://doi.org/10.1016/j.neucom.2023.126482>. URL <https://www.sciencedirect.com/science/article/pii/S0925231223006057>
- [7] J. Ma, X. Jiang, A. Fan, J. Jiang, J. Yan, Image matching from handcrafted to deep features: A survey, *Int. J. Comput. Vision* 129 (1) (2021) 237–279. doi:[10.1007/s11263-020-01359-2](https://doi.org/10.1007/s11263-020-01359-2). URL <https://doi.org/10.1007/s11263-020-01359-2>
- [8] P. J. Besl, N. D. McKay, A method for registration of 3-d shapes, *IEEE Trans. Pattern Analysis and Machine Intelligence* 14 (2) (1992) 239–256.
- [9] C. Zhang, S. Du, J. Liu, Y. Li, J. Xue, Y. Liu, Robust iterative closest point algorithm with bounded rotation angle for 2d registration, *Neurocomputing* 195 (2016) 172–180.
- [10] L. Liang, Precise iterative closest point algorithm for rgb-d data registration with noise and outliers, *Neurocomputing* 399 (2020) 361–368.
- [11] M. Sofka, G. Yang, C. V. Stewart, Simultaneous covariance driven correspondence (cdc) and transformation estimation in the expectation maximization framework, in: *IEEE Conf. Computer Vision and Pattern Recognition*, 2007, pp. 1–8.
- [12] J. Ma, W. Qiu, J. Zhao, Y. Ma, A. L. Yuille, Z. Tu, Robust l_2e estimation of transformation for non-rigid registration, *IEEE Transactions on Signal Processing* 63 (5) (2015) 1115–1129. doi:[10.1109/TSP.2014.2388434](https://doi.org/10.1109/TSP.2014.2388434).
- [13] A. Myronenko, X. Song, Point set registration: Coherent point drift, *IEEE Transactions on Pattern Analysis and Machine Intelligence* 32 (12) (2010) 2262–2275.
- [14] B. Jian, B. C. Vemuri, Robust point set registration using gaussian mixture models, *IEEE Trans. Pattern Analysis and Machine Intelligence* 33 (8) (2011) 1633–1645.
- [15] D. Campbell, L. Petersson, An adaptive data representation for robust point-set registration and merging, in: *2015 IEEE International Conference on Computer Vision (ICCV)*, 2015, pp. 4292–4300. doi:[10.1109/ICCV.2015.488](https://doi.org/10.1109/ICCV.2015.488).
- [16] W. Gao, R. Tedrake, Filterreg: Robust and efficient probabilistic point-set registration using gaussian filter and twist parameterization, in: *2019 IEEE/CVF Conference on Computer Vision and Pattern Recognition (CVPR)*, 2019, pp. 11087–11096. doi:[10.1109/CVPR.2019.01135](https://doi.org/10.1109/CVPR.2019.01135).
- [17] F. J. Lawin, M. Danelljan, F. S. Khan, P.-E. Forssten, M. Felsberg, Density adaptive point set registration, in: *2018 IEEE/CVF Conference on Computer Vision and Pattern Recognition*, 2018, pp. 3829–3837. doi:[10.1109/CVPR.2018.00403](https://doi.org/10.1109/CVPR.2018.00403).
- [18] B. Eckart, K. Kim, J. Kautz, Hgmr: Hierarchical gaussian mixtures for adaptive 3d registration, in: *European Conference on Computer Vision*, Springer International Publishing, 2018, pp. 730–746.
- [19] H. Li, R. Hartley, The 3d-3d registration problem revisited, in: *International Conference on Computer Vision*, 2007.
- [20] J. Yang, H. Li, D. Campbell, Y. Jia, Go-icp: A globally optimal solution to 3d icp point-set registration, *IEEE Transactions on Pattern Analysis and Machine Intelligence* 38 (11) (2016) 2241–2254. doi:[10.1109/TPAMI.2015.2513405](https://doi.org/10.1109/TPAMI.2015.2513405).
- [21] D. Campbell, L. Petersson, Gogma: Globally-optimal gaussian mixture alignment, in: *The IEEE Conference on Computer Vision and Pattern Recognition*, 2016.
- [22] Á. Parra, T.-J. Chin, A. Eriksson, H. Li, D. Suter, Fast rotation search with stereographic projections for 3d registration, *IEEE Transactions on Pattern Analysis and Machine Intelligence* 38 (11) (2016) 2227–2240.
- [23] J. Straub, T. Campbell, J. P. How, J. W. Fisher, Efficient global point cloud alignment using bayesian nonparametric mixtures, in: *2017 IEEE Conference on Computer Vision and Pattern Recognition (CVPR)*, 2017, pp. 2403–2412. doi:[10.1109/CVPR.2017.258](https://doi.org/10.1109/CVPR.2017.258).
- [24] Q.-Y. Zhou, J. Park, V. Koltun, Fast global registration, in: *European Conference on Computer Vision*, Springer International Publishing, Cham, 2016, pp. 766–782.
- [25] Á. Parra, T.-J. Chin, Guaranteed outlier removal for point cloud registration with correspondences, *TPAMI* 40 (12) (2018) 2868–2882.
- [26] H. Yang, J. Shi, L. Carlone, Teaser: Fast and certifiable point cloud registration, *IEEE Transactions on Robotics* (2020) 1–20. doi:[10.1109/TR0.2020.3033695](https://doi.org/10.1109/TR0.2020.3033695).
- [27] Y. Aoki, H. Goforth, R. A. Srivatsan, S. Lucey, Pointnetlk: Robust and efficient point cloud registration using pointnet, in: *2019 IEEE/CVF Conference on Computer Vision and Pattern Recognition (CVPR)*, 2019, pp. 7156–7165. doi:[10.1109/CVPR.2019.00733](https://doi.org/10.1109/CVPR.2019.00733).
- [28] X. Huang, G. Mei, J. Zhang, Feature-metric registration: A fast semi-supervised approach for robust point cloud registration without correspondences, in: *Proceedings of the IEEE/CVF Conference on Computer Vision and Pattern Recognition (CVPR)*, 2020.
- [29] C. Choy, J. Park, V. Koltun, Fully convolutional geometric features, in: *2019 IEEE/CVF International Conference on Computer Vision (ICCV)*, 2019, pp. 8957–8965. doi:[10.1109/ICCV.2019.00905](https://doi.org/10.1109/ICCV.2019.00905).
- [30] Z. Gojcic, C. Zhou, J. D. Wegner, W. Andreas, The perfect match: 3d point cloud matching with smoothed densities, in: *International conference on computer vision and pattern recognition (CVPR)*, 2019.
- [31] C. Choy, W. Dong, V. Koltun, Deep global registration, in: *CVPR*, 2020.
- [32] Y. Wang, J. Solomon, Deep closest point: Learning representations for point cloud registration, in: *2019 IEEE/CVF International Conference on Computer Vision (ICCV)*, 2019, pp. 3522–3531. doi:[10.1109/ICCV.2019.00362](https://doi.org/10.1109/ICCV.2019.00362).
- [33] Y. Wang, Y. Sun, Z. Liu, S. E. Sarma, M. M. Bronstein, J. M. Solomon, Dynamic graph cnn for learning on point clouds, *ACM Trans. Graph.* 38 (5). doi:[10.1145/3326362](https://doi.org/10.1145/3326362). URL <https://doi.org/10.1145/3326362>
- [34] A. Vaswani, N. Shazeer, N. Parmar, J. Uszkoreit, L. Jones, A. N. Gomez, u. Kaiser, I. Polosukhin, Attention is all you need, in: *Proceedings of the 31st International Conference on Neural Information Processing Systems, NIPS'17*, Curran Associates Inc., Red Hook, NY, USA, 2017, pp. 6000–6010.
- [35] Y. Wang, J. M. Solomon, Prnet: Self-supervised learning for partial-

to-partial registration, in: Advances in Neural Information Processing Systems, Vol. 32, Curran Associates, Inc., 2019.

URL <https://proceedings.neurips.cc/paper/2019/file/ebad33b3c9fa1d10327bb55f9e79e2f3-Paper.pdf>

- [36] J. Li, C. Zhang, Z. Xu, H. Zhou, C. Zhang, Iterative distance-aware similarity matrix convolution with mutual-supervised point elimination for efficient point cloud registration, in: Computer Vision–ECCV 2020: 16th European Conference, Glasgow, UK, August 23–28, 2020, Proceedings, Part XXIV 16, Springer, 2020, pp. 378–394.
- [37] Y. Shen, L. Hui, H. Jiang, J. Xie, J. Yang, Reliable inlier evaluation for unsupervised point cloud registration, in: Proceedings of the AAAI Conference on Artificial Intelligence, Vol. 36, 2022, pp. 2198–2206.
- [38] Y. Shu, Z. Hou, B. Xiao, X. Bi, X. Luan, W. Li, Partial-to-partial point cloud registration based on multi-level semantic-structural cognition, in: 2022 IEEE International Conference on Multimedia and Expo (ICME), IEEE, 2022, pp. 1–6.
- [39] A. Volgenant, Solving the k-cardinality assignment problem by transformation, European Journal of Operational Research 157 (2004) 322–331.
- [40] R. Jonker, A. Volgenant, A shortest augmenting path algorithm for dense and sparse linear assignment problems, Computing 38 (1987) 325–340.
- [41] A. Zeng, S. Song, M. Nießner, M. Fisher, J. Xiao, T. Funkhouser, 3dmatch: Learning local geometric descriptors from rgb-d reconstructions, in: CVPR, 2017.
- [42] L. Z. H. F. L. Q. Xuyang Bai, Zixin Luo, C.-L. Tai, D3feat: Joint learning of dense detection and description of 3d local features, arXiv:2003.03164 [cs.CV].

Appendix A. A weak result about positive semidefiniteness of matrix $\mathbf{H}^0 + \mathbf{C}$

Proposition 1. *Matrix $\mathbf{H}^0 + \mathbf{C}$ is close to being positive semidefinite.*

Proof. For any $\mathbf{p} \in \Omega$, it is apparently that $\mathbf{p} \geq 0$. Thus, given $\mathbf{p} \in \Omega$, the function E in equation (3a) is a convex quadratic function of θ . Therefore, from equation (5), we can infer that $\text{mat}(\mathbf{KB}_2\mathbf{p}) + \mathbf{C} \geq 0$ for any $\mathbf{p} \in \Omega$.

Let

$$\mathbf{p}^{ij} = \arg \min_{\mathbf{p} \in \Omega} [\text{mat}(\mathbf{KB}_2\mathbf{p})]_{ij}$$

Apparently $\text{mat}(\mathbf{KB}_2\mathbf{p}^{ij}) + \mathbf{C} \geq 0$. Based on the fact that $\underline{\Gamma}_{ij} = \min_{\mathbf{p} \in \Omega} [\text{mat}(\mathbf{KB}_2\mathbf{p})]_{ij} = \min_{\mathbf{p} \in \{\mathbf{p}^{ij}\}} [\text{mat}(\mathbf{KB}_2\mathbf{p})]_{ij}$, we have that $\underline{\Gamma}$ is close to one of $\text{mat}(\mathbf{KB}_2\mathbf{p}^{ij})$, $\forall i, j$. Consequently $\underline{\Gamma} + \mathbf{C}$ is close to being positive semidefinite.

In an analogous way, let

$$\mathbf{q}^{ij} = \arg \max_{\mathbf{p} \in \Omega} [\text{mat}(\mathbf{KB}_2\mathbf{p})]_{ij}$$

Apparently $\text{mat}(\mathbf{KB}_2\mathbf{q}^{ij}) + \mathbf{C} \geq 0$. Based on $\bar{\Gamma}_{ij} = \max_{\mathbf{p} \in \Omega} [\text{mat}(\mathbf{KB}_2\mathbf{p})]_{ij} = \max_{\mathbf{p} \in \{\mathbf{q}^{ij}\}} [\text{mat}(\mathbf{KB}_2\mathbf{p})]_{ij}$, we have $\bar{\Gamma}$ is close to one of $\text{mat}(\mathbf{KB}_2\mathbf{q}^{ij})$, $\forall i, j$. Consequently $\bar{\Gamma} + \mathbf{C}$ is close to being positive semidefinite.

Therefore $\mathbf{H}^0 + \mathbf{C} = \frac{(\underline{\Gamma} + \mathbf{C}) + (\bar{\Gamma} + \mathbf{C})}{2}$ is close to being positive semidefinite.

□

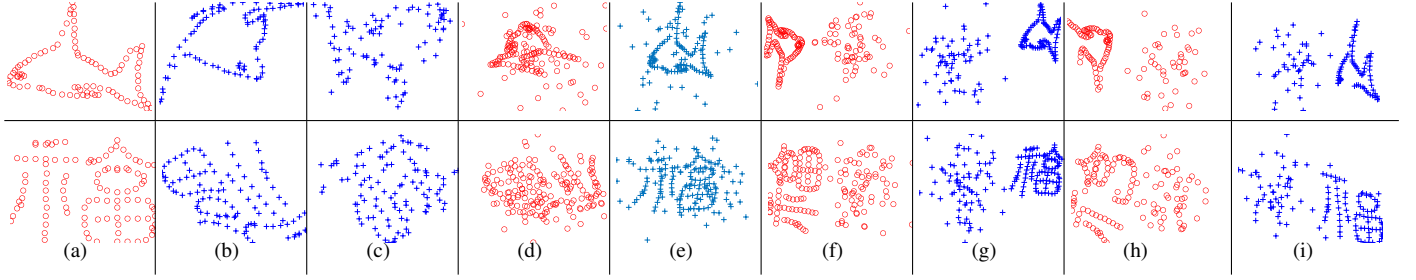


Figure 5: a) to (c): Model point sets and examples of scene point sets in the deformation and noise tests, respectively. (d) to (i): Examples of model and scene point sets in the mixed outliers and inliers test ((d), (e)), separate outliers and inliers test ((f), (g)), and occlusion+outlier test ((h), (i)), respectively. In all cases, model points are indicated by red circles, while scene points are represented by blue crosses.

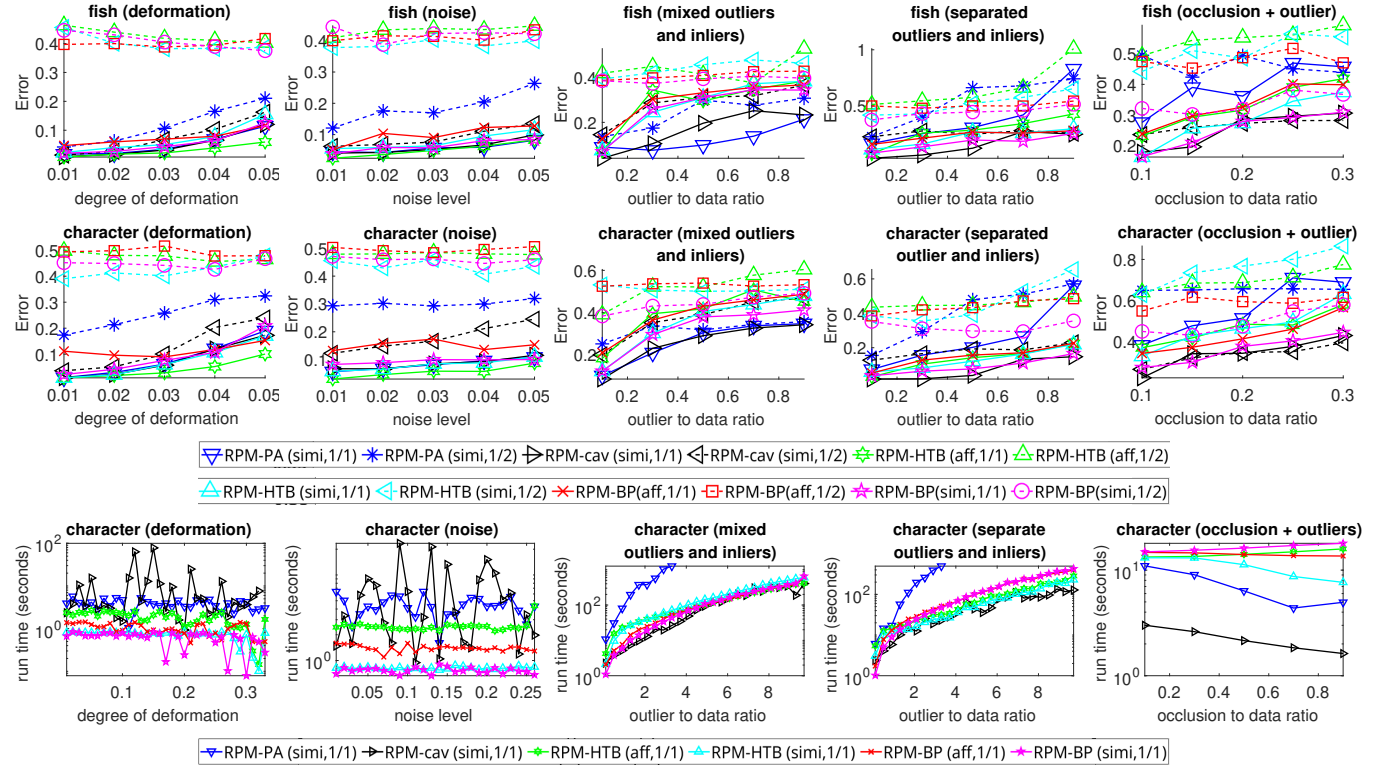
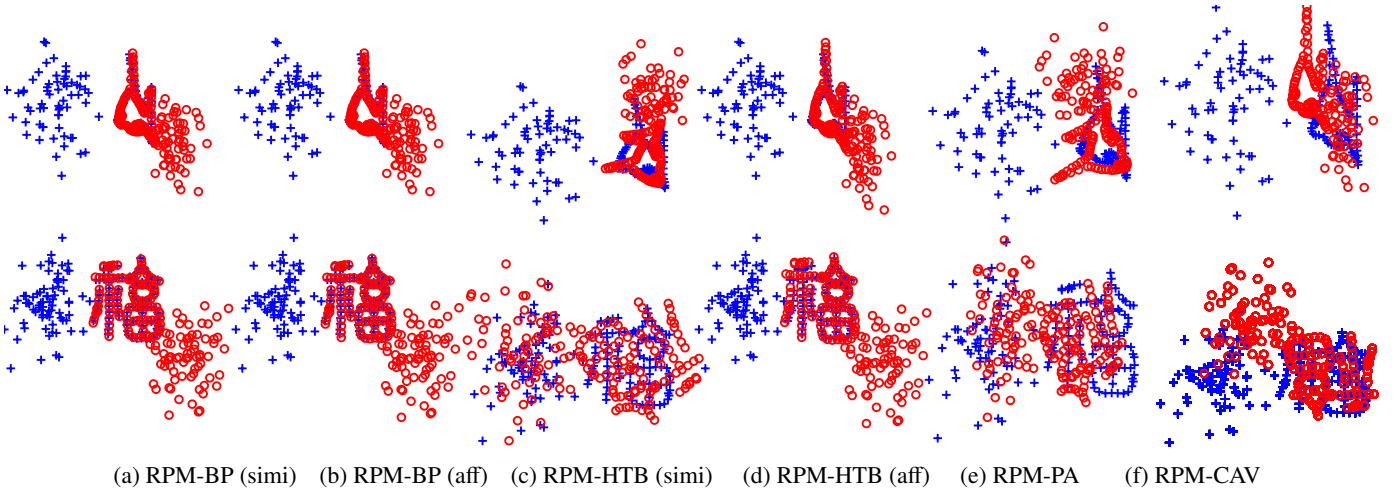


Figure 6: Average registration errors (top 2 rows) and run times (bottom row) by RPM-BP, RPM-HTB [6], and RPM-CAV [4] under various n_p values (ranging from 1/2 to 1/1 of the ground truth value) over 100 random trials for 2D deformation, noise, mixed outliers and inliers, separate outliers and inliers, and occlusion+outlier tests.



(a) RPM-BP (simi) (b) RPM-BP (aff) (c) RPM-HTB (simi) (d) RPM-HTB (aff) (e) RPM-PA (f) RPM-CAV

Figure 7: Example of registration results from different methods in the separate outliers and inliers test, with n_p chosen as ground truth for all methods.

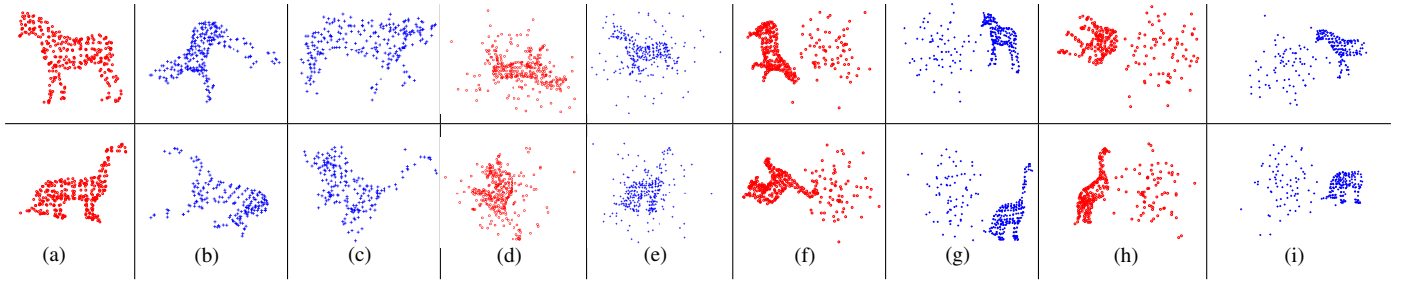


Figure 8: (a) to (c): Model point sets and corresponding examples of scene point sets in the deformation and noise tests, respectively. (d) to (i): Examples of model and scene point sets in the mixed outliers and inliers test ((d), (e)), separate outliers and inliers test ((f), (g)), and occlusion+outlier test ((h), (i)), respectively. In all cases, model points are indicated by red circles, while scene points are represented by blue crosses.

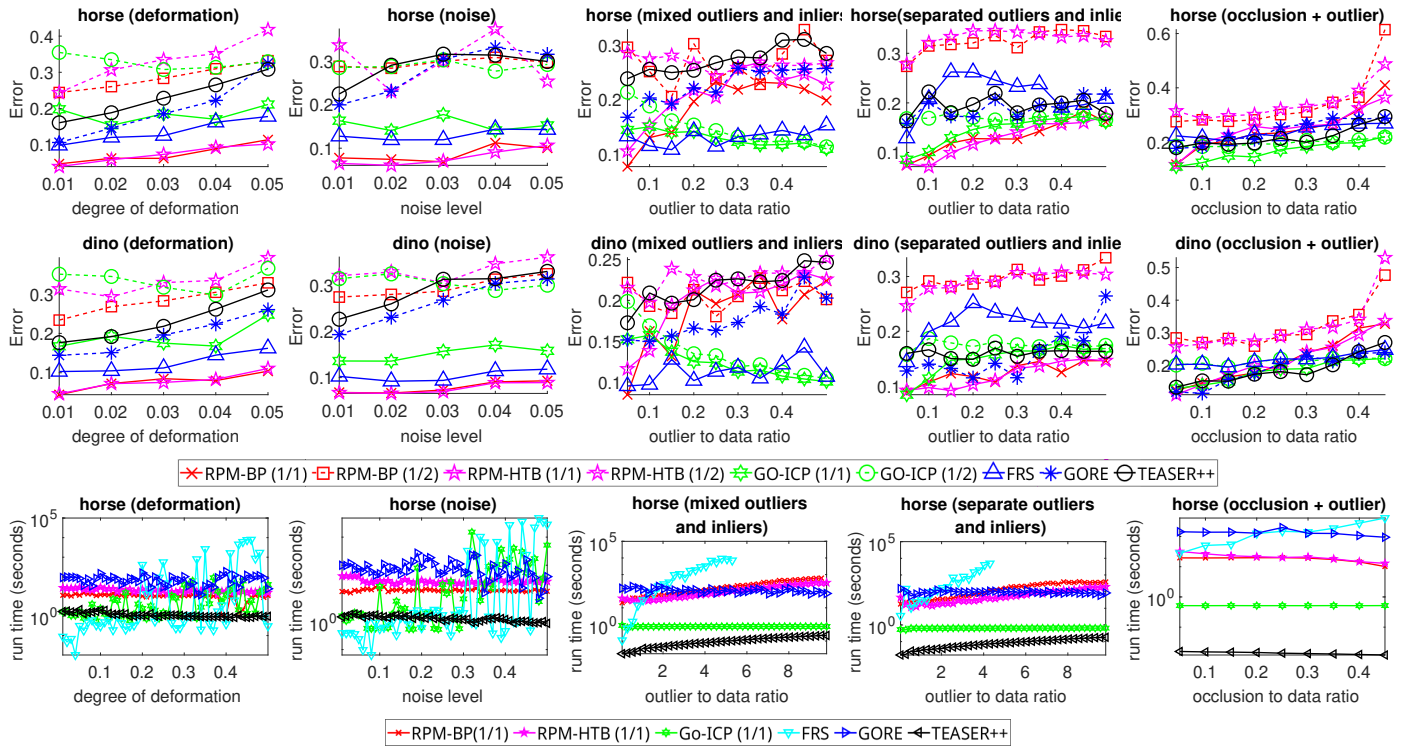


Figure 9: Average registration errors (top 2 rows) and run times (bottom row) of RPM-BP, RPM-HTB, Go-ICP, FRS, GORE, and TEASER++ under varying n_p values (ranging from 1/2 to 1/1 of the ground truth value) across 100 random trials for 3D deformation, noise, mixed outliers and inliers, separate outliers and inliers, and occlusion+outlier tests. For the separate outliers and inliers and occlusion+outlier tests, only a portion of FRS's run time results is presented, as FRS experiences significant slowdowns with large problem sizes.

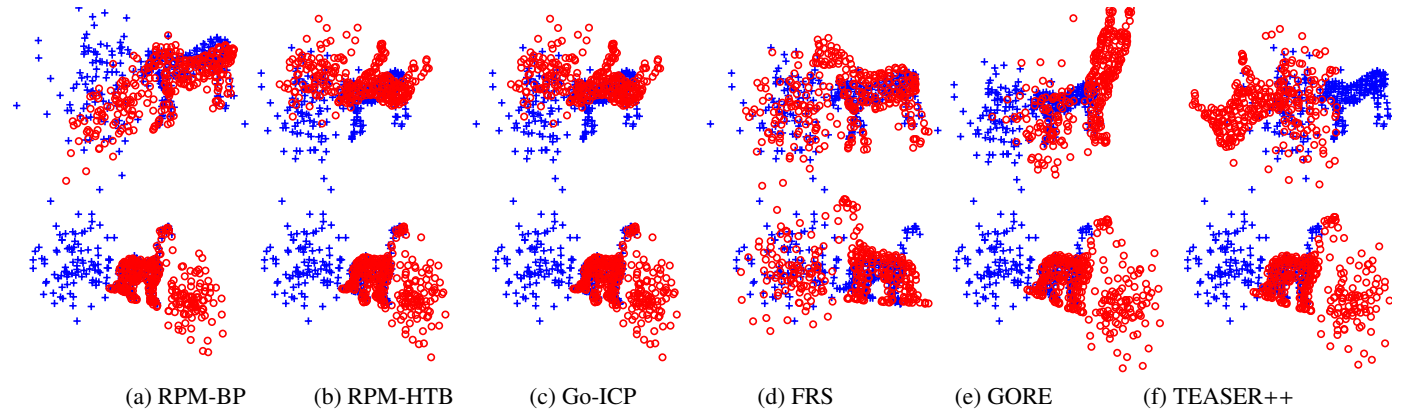


Figure 10: Examples of registration results from different methods in the separate outliers and inliers test, where the n_p values of RPM-HTB and Go-ICP are both chosen to match the ground truth.

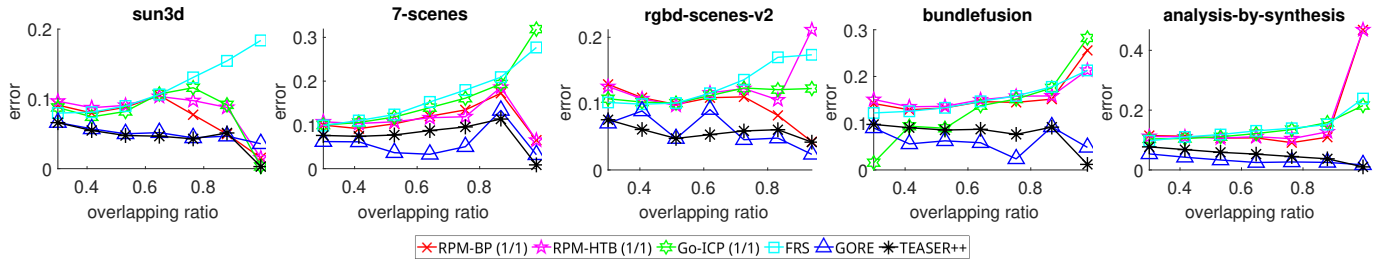


Figure 11: Average registration errors from various methods across five RGB-D reconstruction datasets.

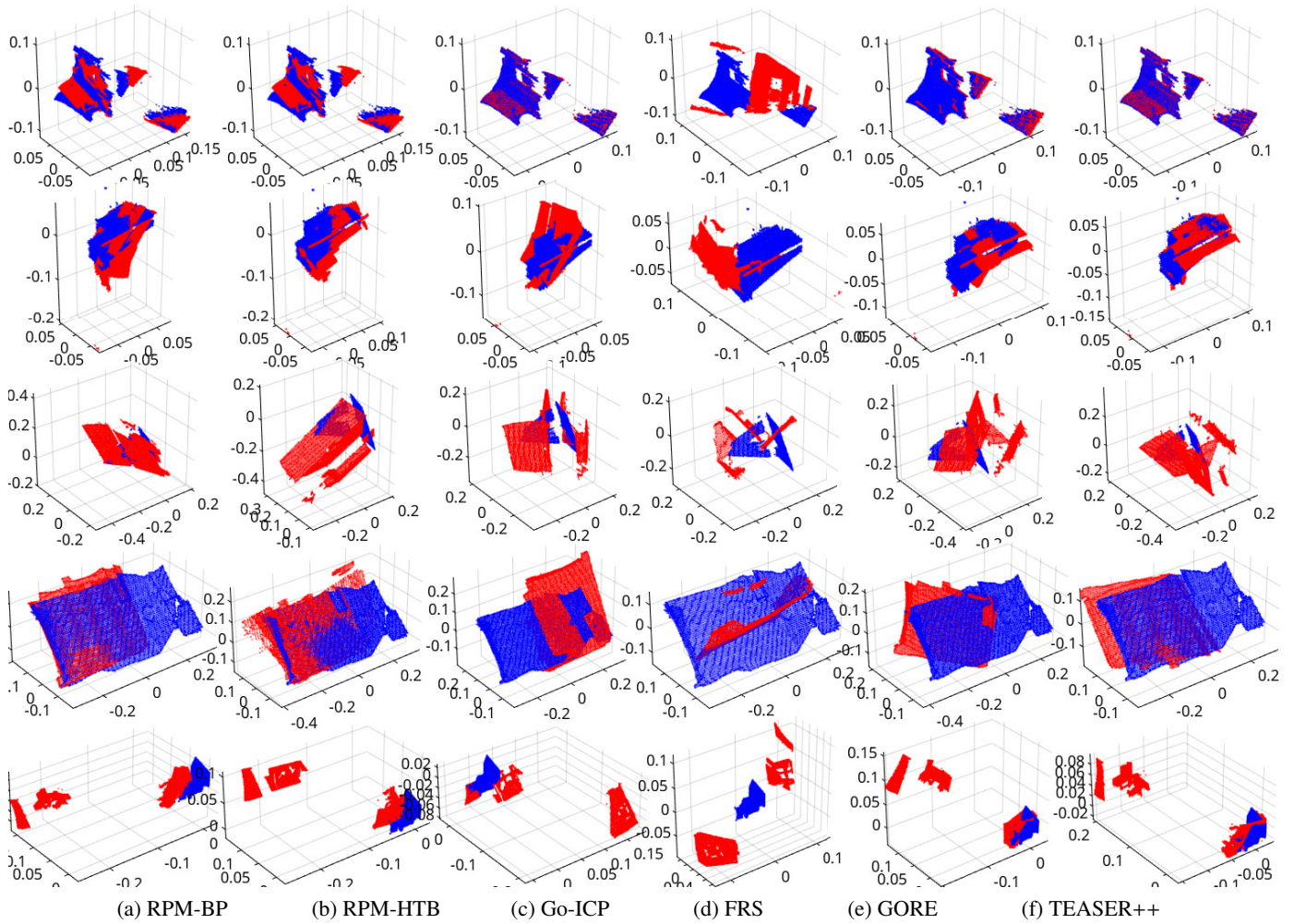


Figure 12: Examples of registration results generated by different methods on the five RGB-D reconstruction datasets, arranged from top to bottom: sun3d, 7-scenes, rgbd-scenes-v2 (repeated), and analysis-by-synthesis.